Laminar and Turbulent Simulations of Several TVD Schemes in Two-Dimensions – Part II

Edisson S. G. Maciel

***Abstract*—**This work, second of this study, describes four numerical tools to perform perfect gas simulations of the laminar and turbulent viscous flow in two-dimensions. The Yee, Warming and Harten, Yee and Kutler, Yee, Warming and Harten and Yee schemes are implemented to accomplish the numerical simulations. The Navier-Stokes equations, on a finite volume context and employing structured spatial discretization, are applied to solve the supersonic flow along a ramp in two-dimensions. Three turbulence models are applied to close the system, namely: Cebeci and Smith, Baldwin and Lomax and Sparlat and Allmaras. All schemes are TVD ("Total Variation Diminishing") ones, where the Yee, Warming and Harten, Yee and Kutler, and Yee, Warming and Harten are derived from a first order upwind scheme and the Yee is derived from a first order symmetrical scheme. The latter reaches TVD properties by the appropriated definition of a limited dissipation function that uses non-linear limiters. The convergence process is accelerated to the steady state condition through a spatially variable time step procedure, which has proved effective gains in terms of computational acceleration (see Maciel). The results have shown that the Yee and Kutler and Yee schemes yield the best results in terms of the prediction of the shock angle at the ramp. Moreover, the wall pressure distribution is also better predicted by the Yee algorithm.

***Keywords*—**Laminar and turbulent flows; TVD algorithms, Cebeci and Smith turbulence model, Baldwin and Lomax turbulence model, Sparlat and Allmaras turbulence model.

I. Introduction

HIGH resolution upwind schemes have been developed since 1959, aiming to improve the generated solution quality, yielding more accurate solutions and more robust codes. The high resolution upwind schemes can be of flux vector splitting type or flux difference splitting type. In the former case, more robust algorithms are yielded, while in the latter case, more accuracy is obtained. Several studies were reported in the international literature involving high resolution algorithms, some of them are compiled below:

[1] supposed that initial data could be replaced by a sort of piecewise constant states with discontinuities in {xi+1/2}. He found the exact solution to this simplified Riemann problem. After some time step Δt, he replaced the exact solution to a new piecewise constant state approximation, while preserving integral properties of the u conserved variable.

[2] developed a class of new finite difference schemes, explicit and with second order of spatial accuracy to calculation of weak solutions of the hyperbolic conservation laws. These schemes highly non-linear were obtained by the application of a first order non-oscillatory scheme to an appropriated modified flux function. The so derived second order schemes reached high resolution, while preserved the robustness property of the original non-oscillatory first order scheme.

[3] implemented a high resolution second order explicit method based on Harten's ideas. The method had the following properties: (a) the scheme was developed in conservation form to ensure that the limit was a weak solution; (b) the scheme satisfied a proper entropy inequality to ensure that the limit solution would have only physically relevant discontinuities; and (c) the scheme was designed such that the numerical dissipation produced highly accurate weak solutions. The method was applied to the solution of a quasi-one-dimensional nozzle problem and to the two-dimensional shock reflection problem, yielding good results. An implicit implementation was also investigated to one- and two-dimensional cases.

[4] applied a new implicit unconditionally stable high resolution TVD scheme to steady state calculations. It was a member of a one-parameter family of explicit and implicit second order accurate schemes developed by [2] for the computation of weak solutions of one-dimensional hyperbolic conservation laws. The scheme was guaranteed not to generate spurious oscillations for a nonlinear scalar equation and a constant coefficient system. Numerical experiments have shown that the scheme not only had a fairly rapid convergence rate, but also generated a highly resolved approximation to the steady state solution. A detailed implementation of the implicit scheme for the one- and two-dimensional compressible inviscid equations of gas dynamics was presented. Some numerical experiments of one- and two-dimensional fluid flows containing shocks demonstrated the efficiency and accuracy of the new scheme.

[5] presented a work which extended the [2] scheme to a generalized coordinate system, in two-dimensions. The method called "TVD scheme" by the authors was tested to the physical problem of a moving shock impinging a cylinder. The numerical results were compared with the [6] scheme, presenting good results.

[7] gives a very extensive survey of the state of the art of second order high resolution schemes for the Euler/Navier-

Edisson S. G. Maciel works as a post-doctorate researcher at ITA (Aeronautical Technological Institute), Aeronautical Engineering Division – Praça Marechal do Ar Eduardo Gomes, 50 – Vila das Acácias – São José dos Campos – SP – Brazil – 12228-900 (corresponding author, phone number: +55 012 99165-3565; e-mail: edisavio@edissonsavio.eng.br).

Stokes equations of gas dynamics in general coordinates for both ideal and equilibrium real gases. Also, excellent reviews on modern upwind conservative shock capturing schemes and upwind shock fitting schemes based on wave propagation property have been given by [8-9], respectively.

This work, second part of this study, describes four numerical tools to perform perfect gas simulations of the laminar and turbulent viscous flow in two-dimensions. The [3-5,10] schemes are implemented to accomplish the numerical simulations. The Navier-Stokes equations, on a finite volume context and employing structured spatial discretization, are applied to solve the supersonic flow along a ramp in two-dimensions. Three turbulence models are applied to close the system, namely: [11], [12] and [13]. All schemes are TVD ones, where the [3-5] are derived from a first order upwind scheme and the [10] is derived from a first order symmetrical scheme. The latter reaches TVD properties by the appropriated definition of a limited dissipation function that uses non-linear limiters. The convergence process is accelerated to the steady state condition through a spatially variable time step procedure, which has proved effective gains in terms of computational acceleration (see [14-15]). The results have shown that the [5,10] schemes yield the best results in terms of the prediction of the shock angle at the ramp. Moreover, the wall pressure distribution is also better predicted by the [10] algorithm.

For an introduction about the motivation of this work, second part of this study, the reader is encouraged to read the first part of this work [16].

II. Navier-Stokes Equations

The flow is modeled by the Navier-Stokes equations, which express the conservation of mass and energy as well as the momentum variation of a viscous, heat conducting and compressible media, in the absence of external forces. These equations are described in detail in [16]. The reader is encouraged to read this reference aiming better understand of the present study.

III. TVD Algorithms

The description of the convective algorithms of [3-5,10] is presented in [17-26] and the reader is encouraged to read these papers to become familiar with all numerical schemes. Hereafter, this paper will present the viscous formulation of both numerical schemes.

The numerical flux vector of the [3] scheme, for instance, is defined by, at the (i+1/2,j) interface:

$$F^{l}_{i+1/2,j} = \left[\left(E^{l}_{e_{i+1/2,j}} - E^{l}_{v_{i+1/2,j}}\right)h_x + \left(F^{l}_{e_{i+1/2,j}} - F^{l}_{v_{i+1/2,j}}\right)h_y\right]V_{i+1/2,j} + \\ + 0.5D^{l}_{YWH}, \quad (1)$$

where: E_e and F_e are the convective or Euler flux vectors, E_v and F_v are the viscous flux vectors, l varies from 1 to 4 (two-dimensional space), h_x and h_y are the metric terms, $V_{i+1/2,j}$ is the interface volume, and D_{YWH} is the Yee, Warming and Harten's dissipation function, defined in [17-18]. The Euler vectors are defined by the convective contributions of the numerical schemes.

The viscous vectors are calculated with the gradients of the conserved and primitive variables keeping constant in each volume and the application of the Green's theorem to change from a volume integral to a surface integral.

The time integration is performed by a time splitting method, which divides the integration in two parts, each one associated with a spatial coordinate direction.

IV. Turbulence Models

A. Turbulence Model of Cebeci and Smith

The problem of the turbulent simulation is in the calculation of the Reynolds stress. Expressions involving velocity fluctuations, originating from the average process, represent six new unknowns. However, the number of equations keeps the same and the system is not closed. The modeling function is to develop approximations to these correlations. To the calculation of the turbulent viscosity according to the [11] model, the boundary layer is divided in internal and external.

Initially, the (ν_w) kinematic viscosity at wall and the ($\tau_{xy,w}$) shear stress at wall are calculated. After that, the (δ) boundary layer thickness, the (δ_{LM}) linear momentum thickness and the (V_{tBL}) boundary layer tangential velocity are calculated. So, the (N) normal distance from the wall to the studied cell is calculated. The N+ term is obtained from:

$$N^{+} = \sqrt{Re}\sqrt{\tau_{xy,w}/\rho_w}\; N/\nu_w\,, \quad (2)$$

where ρw is the wall density. The van Driest damping factor is calculated by:

$$D = 1 - e^{\left(-N^{+}\sqrt{\rho/\rho_w}\,\mu_w/\mu/A^{+}\right)}, \quad (3)$$

with $A^{+} = 26$ and μ_w is the wall molecular viscosity. After that, the (dVt/dN) normal to the wall gradient of the tangential velocity is calculated and the internal turbulent viscosity is given by:

$$\mu_{Ti} = Re\,\rho(\kappa ND)^2\, dVt/dN\,, \quad (4)$$

where κ is the von Kárman constant, which has the value 0.4. The intermittent function of Klebanoff is calculated to the external viscosity by:

$$g_{Kleb}(N) = \left[1 + 5.5\left(N/\delta\right)^6\right]^{-1}. \quad (5)$$

With it, the external turbulent viscosity is calculated by:

$$\mu_{Te} = Re(0.0168)\rho Vt_{BL}\delta_{LM}g_{Kleb}\,. \quad (6)$$

Finally, the turbulent viscosity is chosen from the internal and the external viscosities: $\mu_T = MIN(\mu_{Ti}, \mu_{Te})$.

B. Turbulence model of Baldwin and Lomax

To the calculation of the turbulent viscosity according to the [12] model, the boundary layer is again divided in internal and external. In the internal layer,

$$\mu_{Ti} = \rho l_{mix}^2 \|\omega\| \quad \text{and} \quad l_{mix} = \kappa N\left(1 - e^{-N^+/A_0^+}\right). \tag{7}$$

In the external layer,

$$\mu_{Te} = \rho\alpha C_{cp} F_{wake} F_{Kleb}(N; N_{max}/C_{Kleb}), \tag{8}$$

with:

$$F_{wake} = MIN\left[N_{max} F_{max}; C_{wk} N_{max} U_{dif}^2 / F_{max}\right],$$
$$F_{max} = 1/\kappa\left[\underset{N}{MAX}\left(l_{mix}\|\omega\|\right)\right]. \tag{9}$$

Hence, N_{max} is the value of N where $l_{mix}\|\omega\|$ reached its maximum value and l_{mix} is the Prandtl mixture length. The constant values are: $\kappa = 0.4$, $\alpha = 0.0168$, $A_0^+ = 26$, $C_{cp} = 1.6$, $C_{Kleb} = 0.3$ and $C_{wk} = 1$. F_{Kleb} is the intermittent function of Klebanoff given by:

$$F_{Kleb}(N) = \left[1 + 5.5\left(C_{Kleb} N / N_{max}\right)^6\right]^{-1}, \tag{10}$$

$\|\omega\|$ is the magnitude of the vortex vector and U_{dif} is the maximum velocity value in the boundary layer case. To free shear layers,

$$U_{dif} = \left(\sqrt{u^2 + v^2 + w^2}\right)_{max} - \left(\sqrt{u^2 + v^2 + w^2}\right)_{N=N_{max}}. \tag{11}$$

C. Turbulence model of Sparlat and Allmaras

The purpose of the [13] one-equation model was overcome the algebraic model limitations and, at the same time, to avoid the difficulties in the implementation of the two-equation models or the Reynolds stress equations. This model employs a transport turbulent viscosity to solve the turbulence scaling. Such model takes naturally into account the turbulence and diffusion histories, which improves its accuracy.

The transport equation to the work turbulent kinematic viscosity is described by:

$$\frac{D\tilde{\nu}}{Dt} = c_{b1}\tilde{S}\tilde{\nu} + \frac{1}{\sigma}\left[\nabla \bullet \left((\nu + \tilde{\nu})\nabla\tilde{\nu}\right) + c_{b2}(\nabla\tilde{\nu})^2\right] - c_{w1} f_w(r)\left(\frac{\tilde{\nu}}{N}\right)^2. \tag{12}$$

In this equation, the first term of the right-hand-side is the production contribution to the work kinematic viscosity; the second term is the viscosity diffusion; and the last term is the destruction of the work kinematic viscosity. The turbulent viscosity is defined by:

$$\mu_T = \rho\tilde{\nu} f_{v1}. \tag{13}$$

With the purpose of assuring that $\tilde{\nu}$ becomes equal to $K \times N \times \sqrt{\tau_{xy,w}/\rho_w}$ in the logarithmic layer and in the viscous sub-layer, the f_{v1} damping function is defined by:

$$f_{v1} = \frac{\lambda^3}{\lambda^3 + {c_{v1}}^3} \tag{14}$$

as function of the $\lambda = \tilde{\nu}/\nu$ variable. The $\tilde{S}$ function, representing the deformation work of the mean flow, is determined as follows:

$$\tilde{S} = \left|\frac{\partial u}{\partial y}\right| + \left[\frac{\tilde{\nu}}{(\kappa N)^2} f_{v2}\right], \tag{15}$$

in which f_{v2} has the following expression:

$$f_{v2} = 1 - \frac{\lambda}{1 + \lambda f_{v1}}. \tag{16}$$

The destruction term should disappear at the external region of the boundary layer. [13] purpose the following function to reproduce such behavior:

$$f_w(r) = g\left[\frac{1 + {c_{w3}}^6}{g^6 + {c_{w3}}^6}\right]^{1/6}, \quad g = r + c_{w2}\left(r^6 - r\right);$$
$$r = \frac{\tilde{\nu}}{(\kappa N)^2 \tilde{S}}, \tag{17}$$

with the r argument and the f_w function reaching the value 1.0 at the logarithmic layer and decreasing at the external region. The g function is merely a limiter to prevent f_w high values. The [13] model constants are:

$$c_{b1} = 0{,}1355,\ c_{b2} = 0{,}622,\ c_{w2} = 0{,}3,\ c_{v1} = 7{,}1;$$
$$\sigma = 2/3,\ c_{w3} = 2{,}0,\ c_{w1} = \frac{c_{b1}}{\kappa^2} + \frac{(1 + c_{b2})}{\sigma}. \tag{18}$$

The [7] model is marched in time using a LU-SGS ("Lower-Upper Factorization – Symmetrical Gauss-Seidel") implicit method. Details of the implicit implementation in two-dimensions are found in [13]. The extension to three-dimensions is straightforward.

In this work, the term referent to the diffusion of the work kinematic viscosity was not implemented. The studied model considers only the production and dissipation terms of the work kinematic viscosity.

V. Spatially Variable Time Step

The basic idea of the spatially variable time step procedure consists in keeping constant the CFL number in all calculation domain, allowing, hence, the use of appropriated time steps to each specific mesh region during the convergence process. In this work, a convective + diffusive option of spatially variable time step calculated at each iteration was studied. Details of the present implementation, see [16].

VI. Initial and Boundary Conditions

A. Initial Condition

Freestream values, at all grid cells, are adopted for all flow properties as initial condition, as suggested by [27].

B. Boundary Conditions

The boundary conditions are basically of three types: solid wall, entrance, and exit. These conditions are implemented in ghost cells. Details of the present implementation, see [16].

VII. Results

One problem was studied in this work, namely: the viscous supersonic flow along a ramp geometry. The ramp configuration is detailed as also the type of boundary contours. These configuration characteristics are described in Figs. 1 and 2. Numerical experiments were run on a Notebook computer with Intel Core i7 processor of 2.3GHz of clock and 8.0 GBytes of RAM. The criterion adopted to reach the steady state was to consider a reduction of three (3) orders of magnitude in the value of the maximum residual in the calculation domain, a typical CFD community criterion. The maximum residual is defined as the maximum value obtained from the discretized equations in the overall domain, considering all conservation equations. The initial conditions to the ramp problem are described in Tab. 1. The number of cells and nodes for the ramp problem are presented in Tab. 2. A mesh of 61x60 nodes, in a finite difference context, is employed.

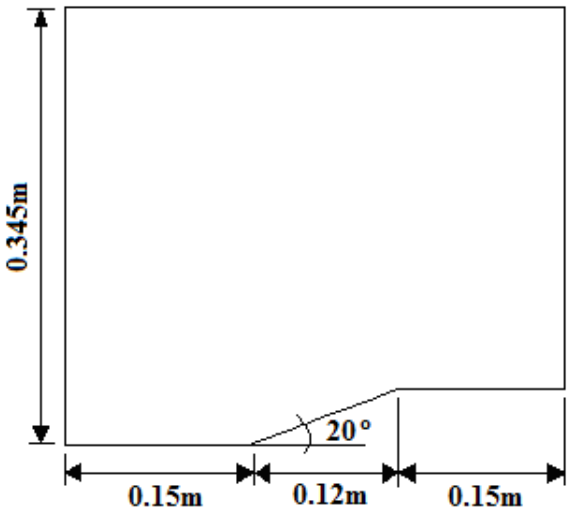

Figure 1. Ramp Configuration.

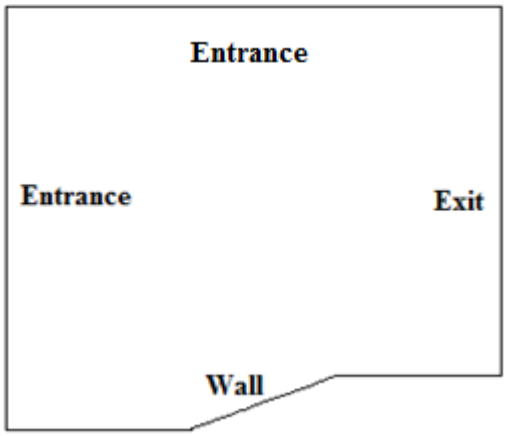

Figure 2. Ramp Computational Domain.

Table 1. Initial Conditions to the Studied Problem.

Problem:	Property:	Value:
Ramp	Freestream Mach, M∞	2.0
	Attack angle, °	0.0
	Ratio of specific heats, γ	1.4

Table 2. Cells and Nodes of the Mesh.

Problem:	Number of rectangular cells:	Number of nodes:
Ramp	3,540	3,660

Figure 3 exhibits the mesh employed in the calculation of the viscous flow to the ramp problem. An exponential stretching of 10.0% was applied close to the wall, in the η direction, to capture the viscous phenomena.

The Reynolds number is equal to 1.613×10^5, a turbulent flow. Three turbulence models will be studied, namely: [11-13]. Two algebraic and an one-equation models are implemented.

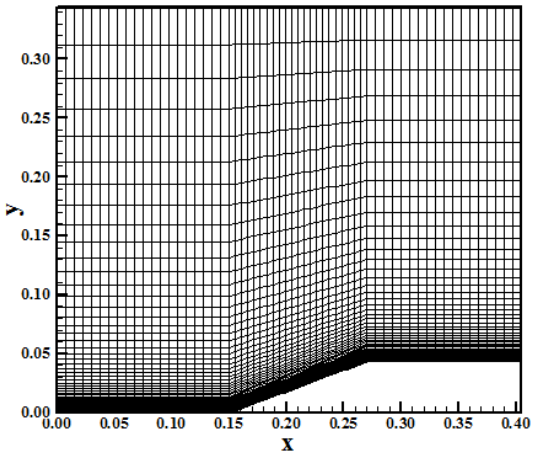

Figure 3. Ramp viscous mesh.

A. Laminar Viscous Results

The second order laminar viscous results are presented here to serve as a benchmark to compare the second order turbulent results, aiming to distinguish the main characteristics of each turbulent model, as referenced by the CFD literature, and verify their potentialities.

TVD High Resolution Results. A minmod like non-linear limiter was employed in the [10] scheme. Figures 4 to 7 exhibit the pressure contours obtained by the [3-5,10] schemes. All solutions present a weak shock ahead of the ramp corner.

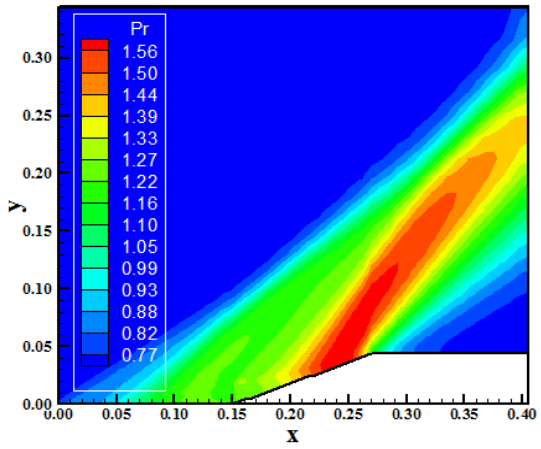

Figure 4. Pressure contours (YWH82).

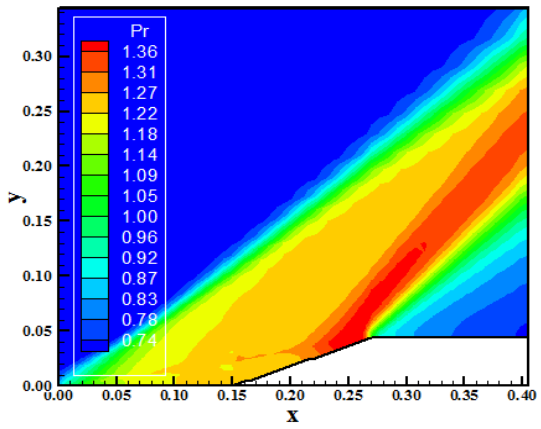

Figure 5. Pressure contours (YWH85).

This shock wave is formed far ahead the ramp corner. The pressure field is also more severe in the solution obtained by the [10] scheme, indicating this one as more conservative.

Figures 8 to 11 show the Mach number contours obtained by the [3-5,10] algorithms. All solutions present a significant region of the detached boundary layer. The most intense Mach number field is obtained by the [4] scheme. In qualitative terms there are meaningful differences. The [4] solution presents the biggest circulation bubble.

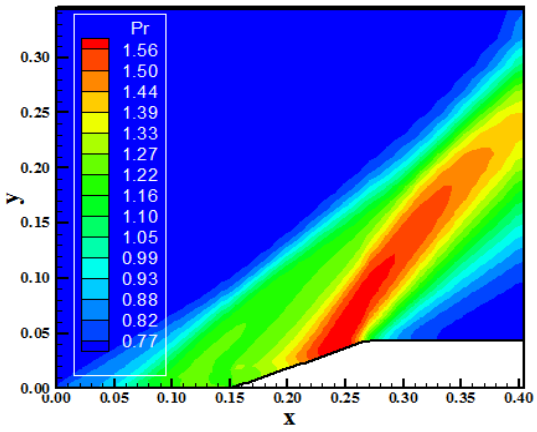

Figure 6. Pressure contours (YK).

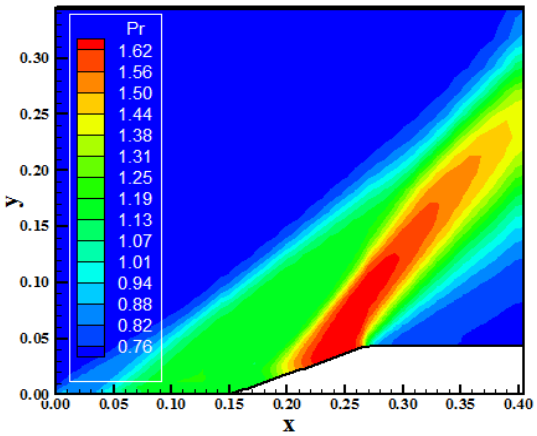

Figure 7. Pressure contours (Yee).

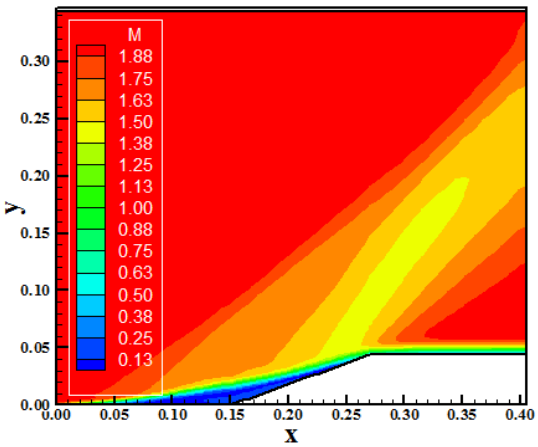

Figure 8. Mach number contours (YWH82).

Figure 12 shows the wall pressure distributions generated by the [3-5,10] schemes. All solutions capture the circulation bubble formation, resulting from the boundary layer detachment. The [10] solution presents a pressure distribution closer to the pressure plateau and the [4] solution presents a more extent separation region.

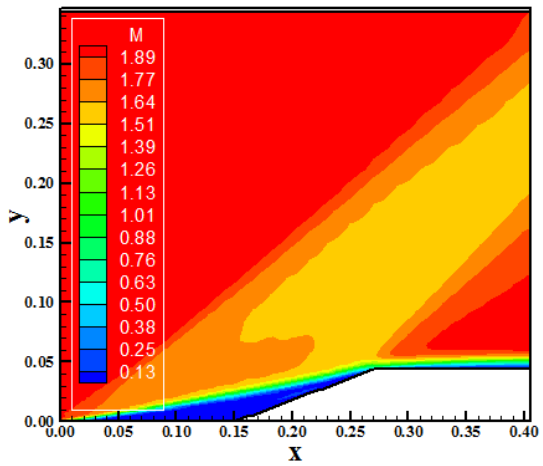

Figure 9. Mach number contours (YWH85).

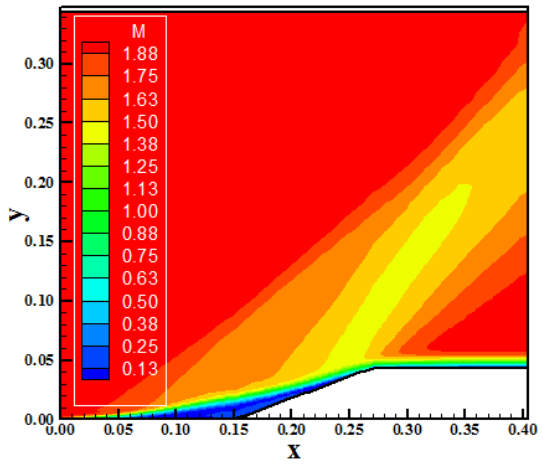

Figure 10. Mach number contours (YK).

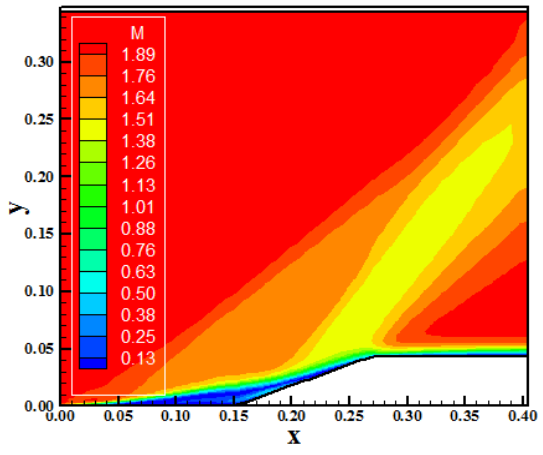

Figure 11. Mach number contours (Yee).

Figures 13 to 16 presents the formation of circulation bubble closes to the ramp corner obtained by [3-5,10] schemes. All schemes present circulation bubbles with the same extension.

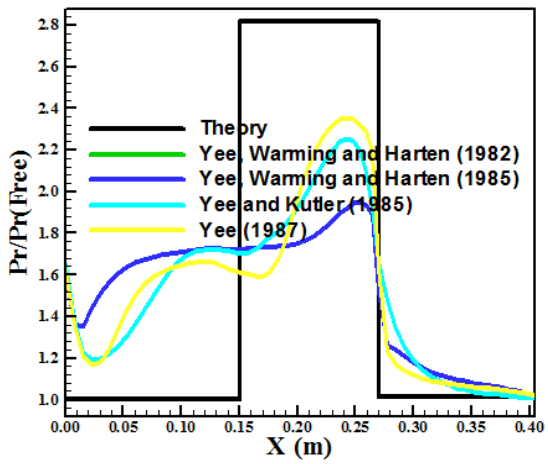

Figure 12. Wall pressure distributions.

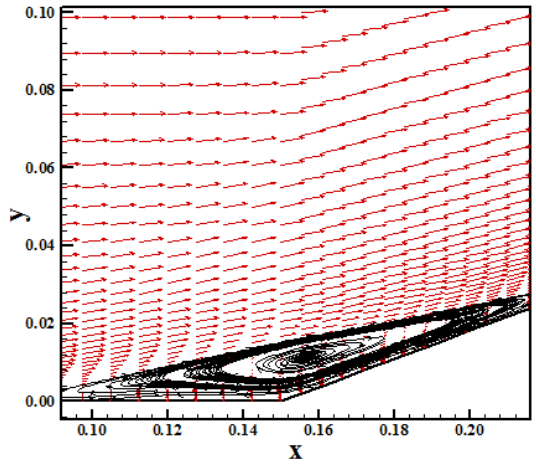

Figure 13. Circulation bubble (YWH82).

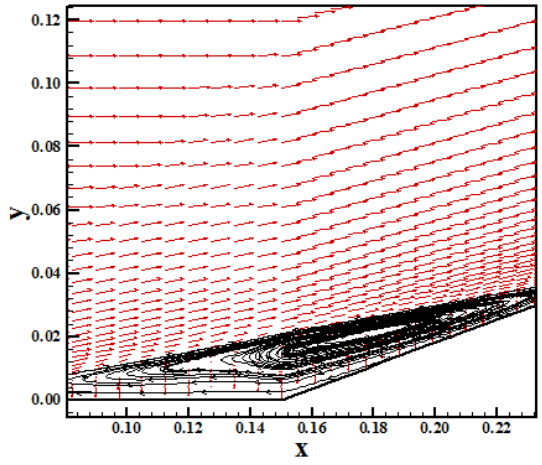

Figure 14. Circulation bubble (YWH85).

As a resume of the present simulations, the [10] scheme was more conservative and more correct in physical terms, representing accurately the flow physics.

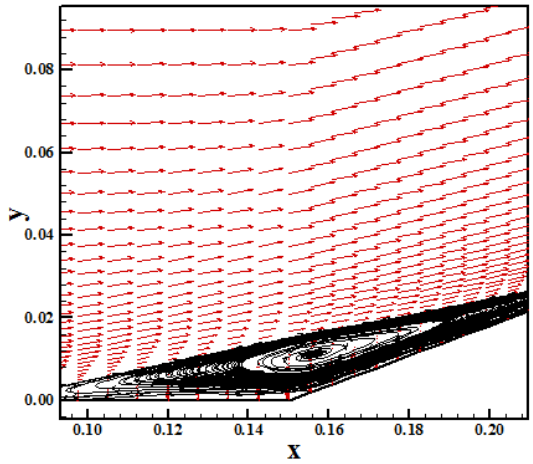

Figure 15. Circulation bubble (YK).

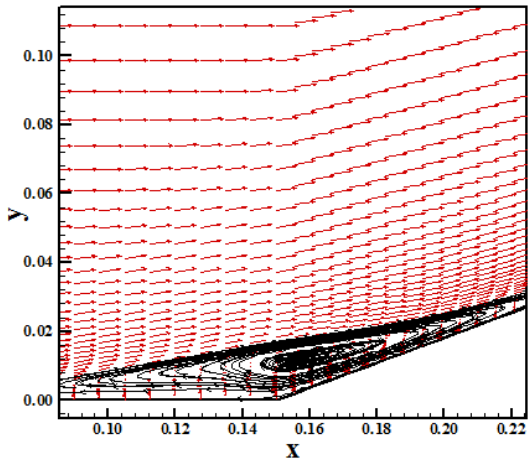

Figure 16. Circulation bubble (Yee).

B. Turbulent Viscous Results

Cebeci and Smith Results. Figures 17 to 20 show the pressure contours obtained by the [3-5,10] schemes, respectively, as using the [11] turbulence model.

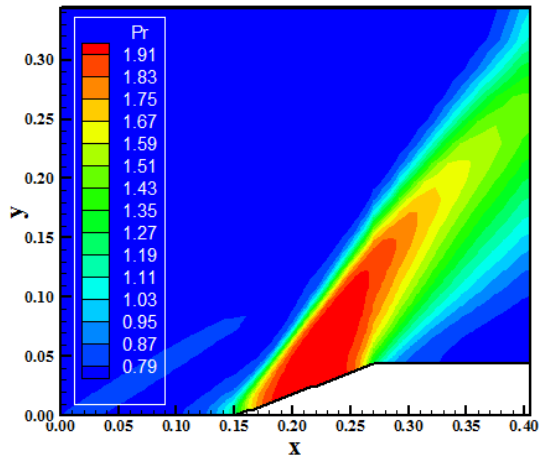

Figure 17. Pressure contours (YWH82-CS).

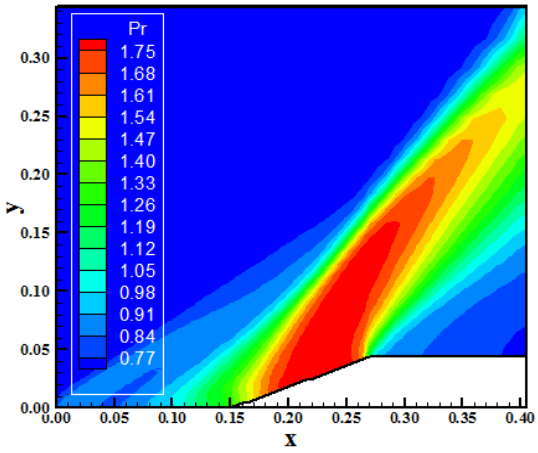

Figure 18. Pressure contours (YWH85-CS).

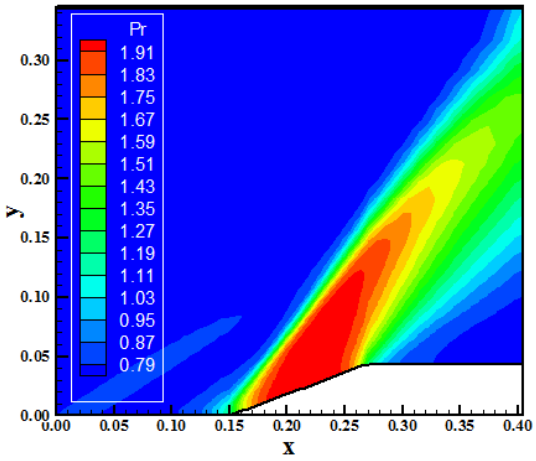

Figure 19. Pressure contours (YK-CS).

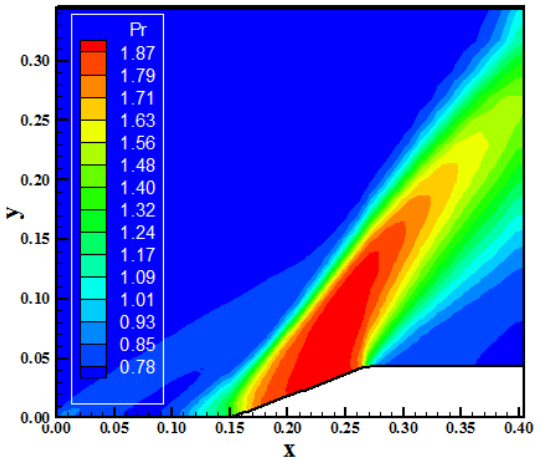

Figure 20. Pressure contours (Yee-CS).

With the exception of the [4] solution, all other solutions practically ignore the existence of the weak shock ahead of the ramp corner. It indicates that the boundary layer detachment is negligible in these solutions and that the circulation bubble is

reduced in size. The pressure field generated by the [3,5] schemes are more severe than the other solutions.

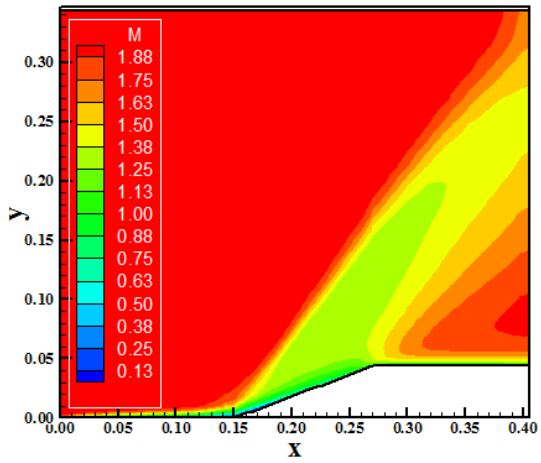

Figure 21. Mach number contours (YWH82-CS).

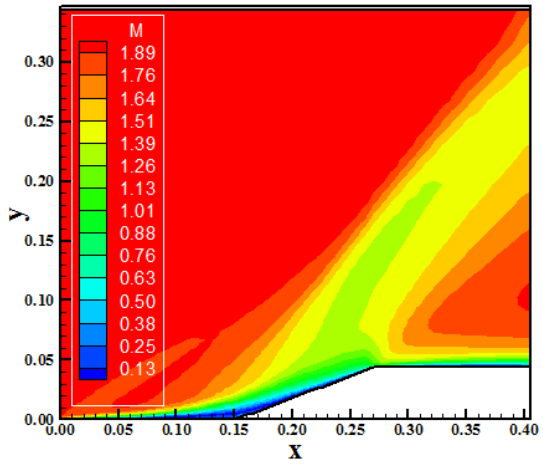

Figure 22. Mach number contours (YWH85-CS).

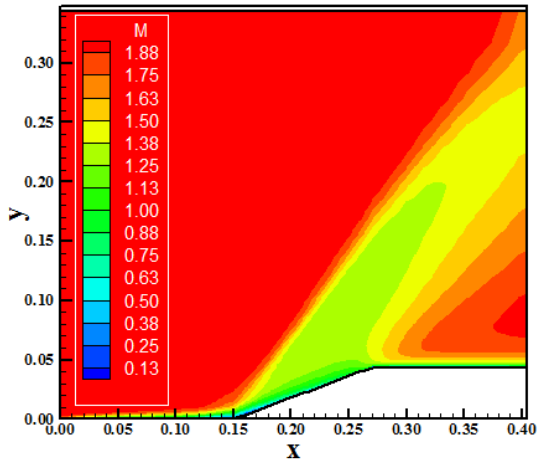

Figure 23. Mach number contours (YK-CS).

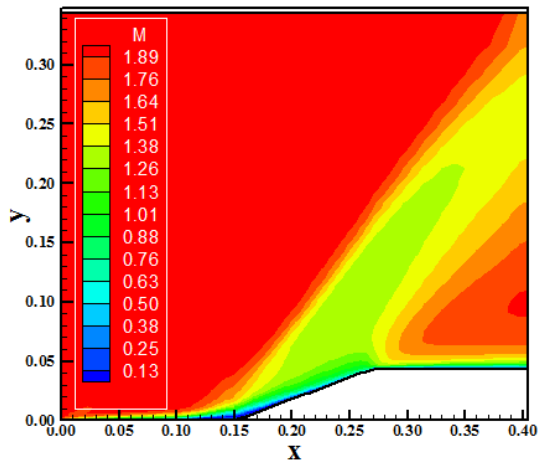

Figure 24. Mach number contours (Yee-CS).

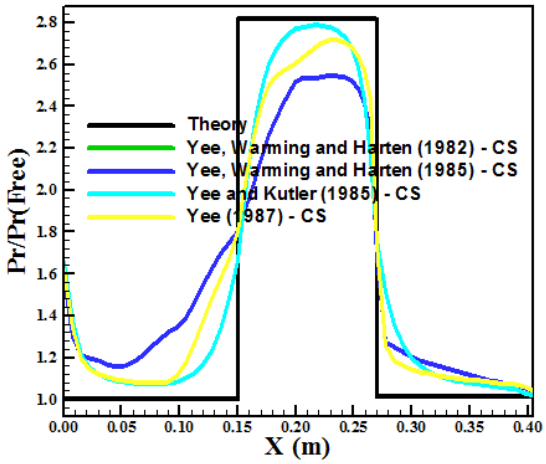

Figure 25. Wall pressure distributions.

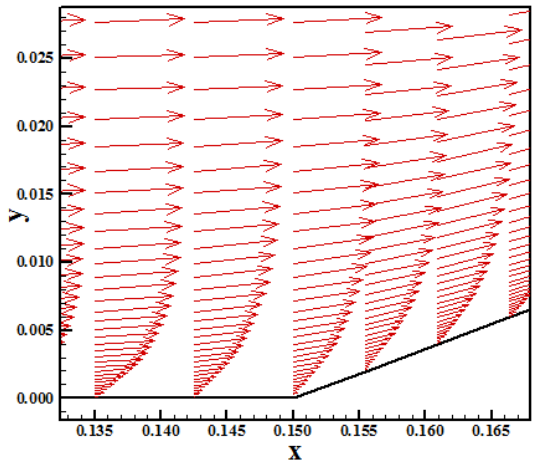

Figure 26. Circulation bubble (YWH82-CS).

Figure 25 exhibits the wall pressure distributions obtained by the [3-5,10] algorithms, as using the [11] turbulence model. As can be observed, the [3,5] solutions are very similar and agree better with the theoretical solution than in the laminar

case. The expansion fan pressure is better predicted by the [3] algorithm.

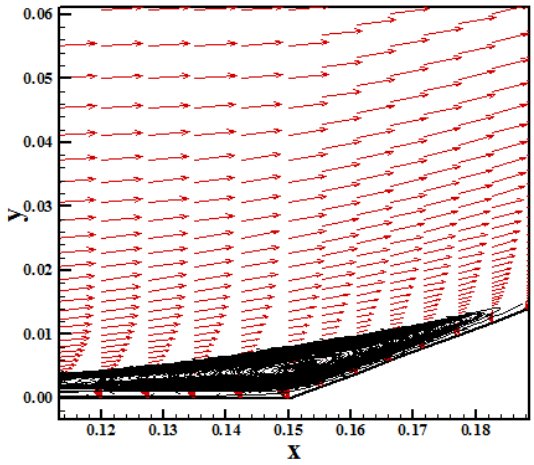

Figure 27. Circulation bubble (YWH85-CS).

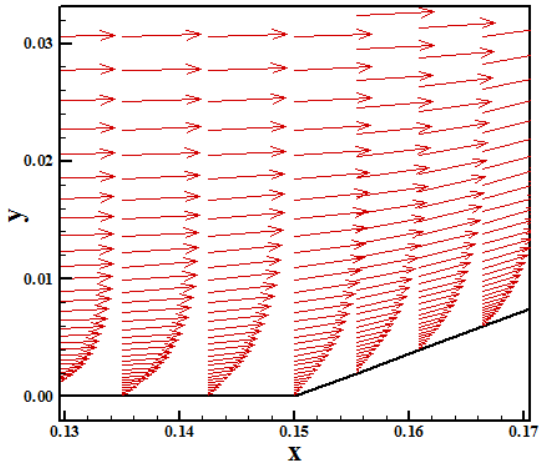

Figure 28. Circulation bubble (YK-CS).

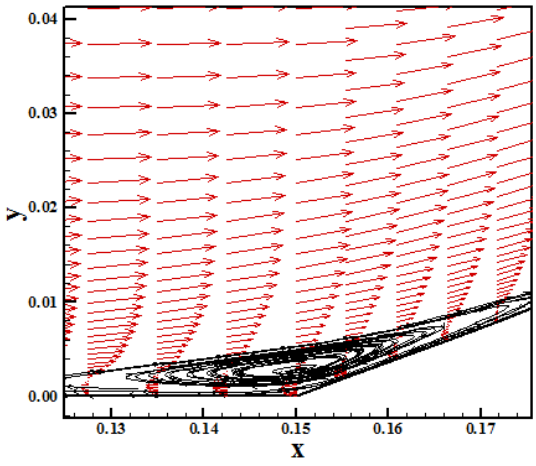

Figure 29. Circulation bubble (Yee-CS).

Figures 26 to 29 show the circulation bubble formation close to the ramp corner. The [4,10] solutions predicted a small circulation bubble, whereas the [3,5] schemes predicted no flow separation.

In resume, as can be observed the [11] turbulence model predicts a more energized boundary layer. With it, the weak shock wave ahead of the ramp corner is negligible and the circulation bubble presents a discrete formation, when occurring.

Baldwin and Lomax Results. Figures 30 to 33 exhibit the pressure contours obtained by the [3-5,10] schemes, respectively, as using the [12] turbulence model. A weak shock wave is formed ahead of the ramp corner in all solutions. It is important to remember that such weak shock wave is due to the boundary layer detachment which induces a false thick geometry at the ramp and the flow only see this thick geometry, originating the oblique shock wave.

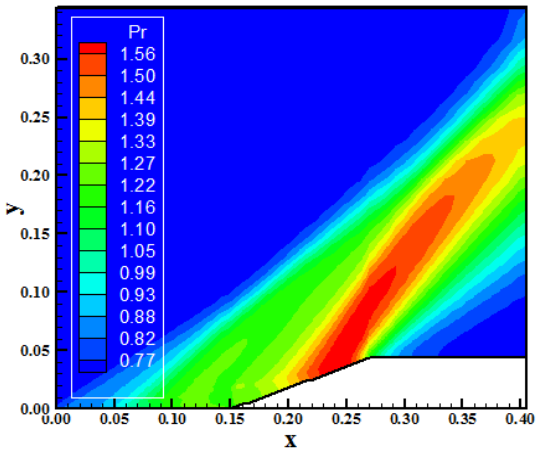

Figure 30. Pressure contours (YWH82-BL).

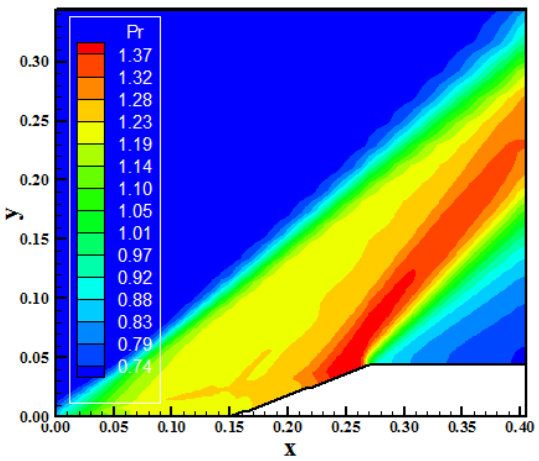

Figure 31. Pressure contours (YWH85-BL).

So, it is possible to verify that the effect of increasing boundary layer thickness is significant in both solutions. In terms of the pressure field, the [10] scheme again presents the most severe pressure field, characterizing this algorithm as the most conservative.

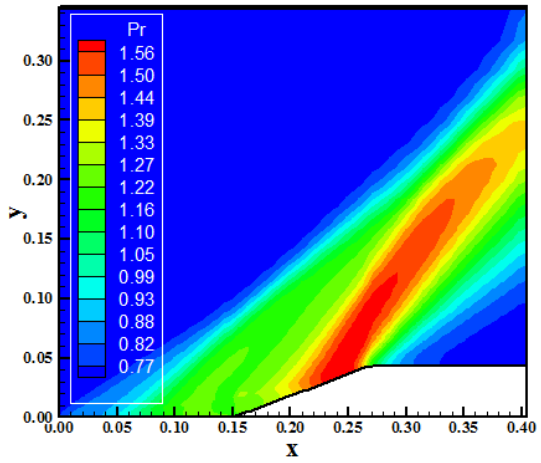

Figure 32. Pressure contours (YK-BL).

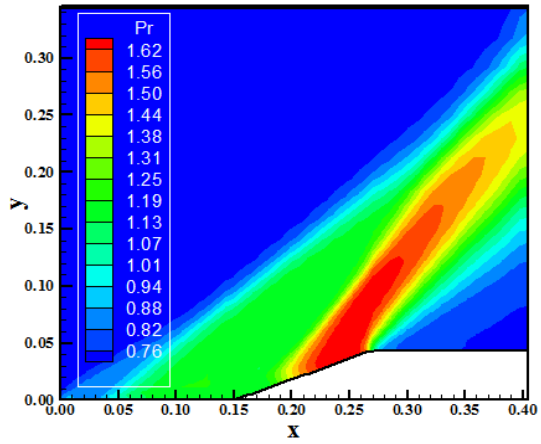

Figure 33. Pressure contours (Yee-BL).

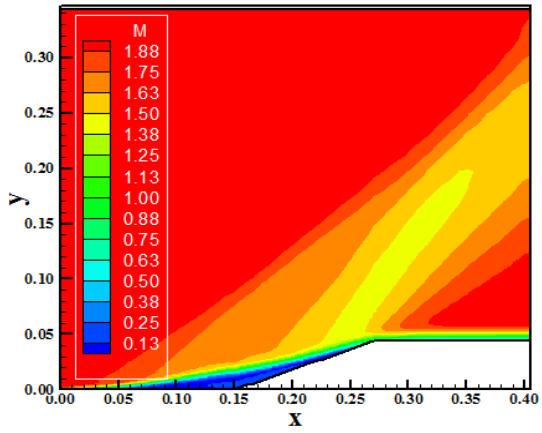

Figure 34. Mach number contours (YWH82-BL).

Figures 34 to 37 show the Mach number contours obtained by the [3-5,10] numerical algorithms, respectively, as using the [12] turbulence model. It is possible to observe that the boundary layer detachment is bigger in the [4] solution, with the consequent formation of a bigger circulation bubble than the other solutions. The Mach number field of the [4] solution is also more severe than the respective of the other solutions.

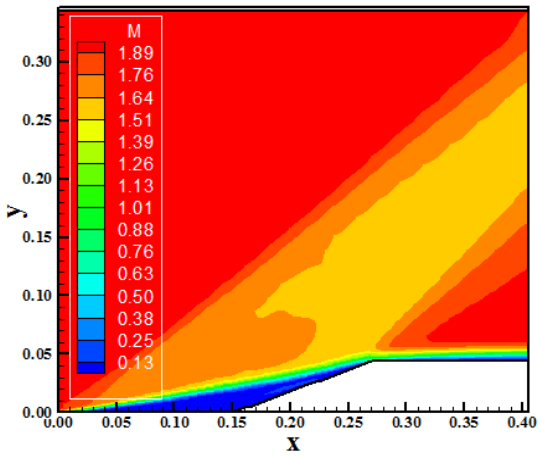

Figure 35. Mach number contours (YWH85-BL).

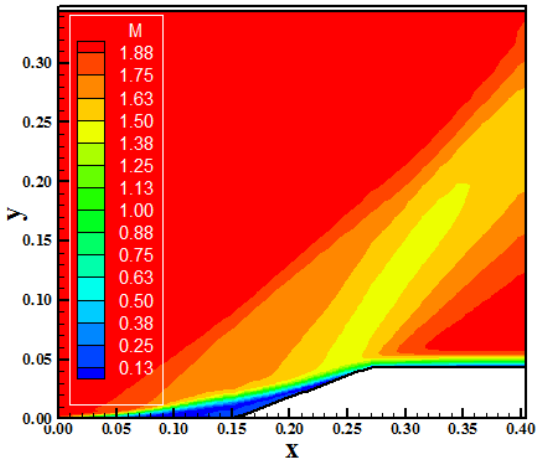

Figure 36. Mach number contours (YK-BL).

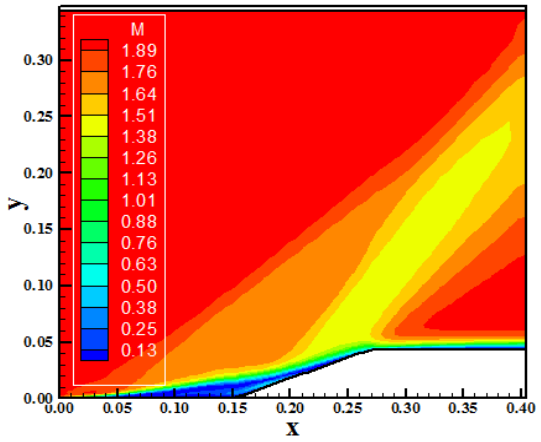

Figure 37. Mach number contours (Yee-BL).

Figure 38 presents the wall pressure distributions generated by all algorithms. As noted, all solutions capture the circulation bubble formation closes to the ramp corner, but all

solutions differs from the theoretical solution (both under-predict the shock plateau).

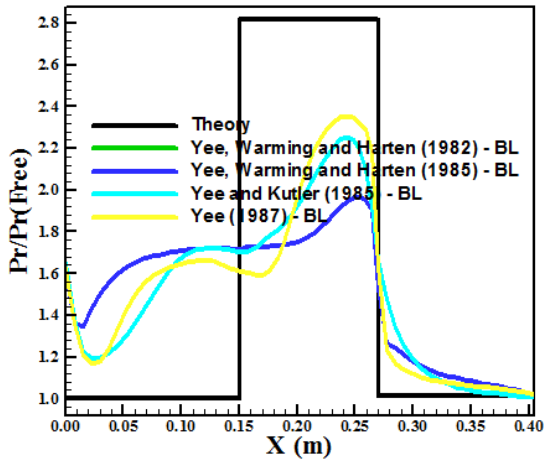

Figure 38. Wall pressure distributions.

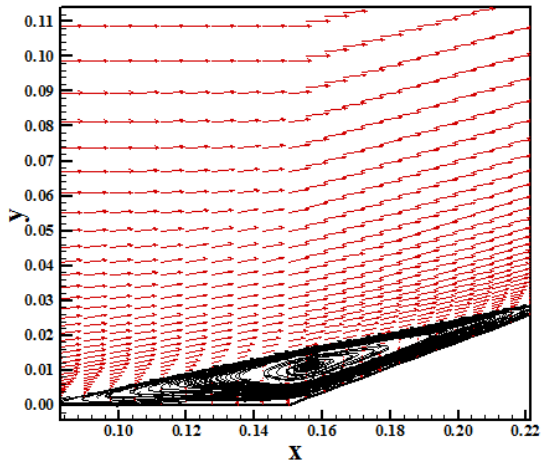

Figure 39. Circulation bubble (YWH82-BL).

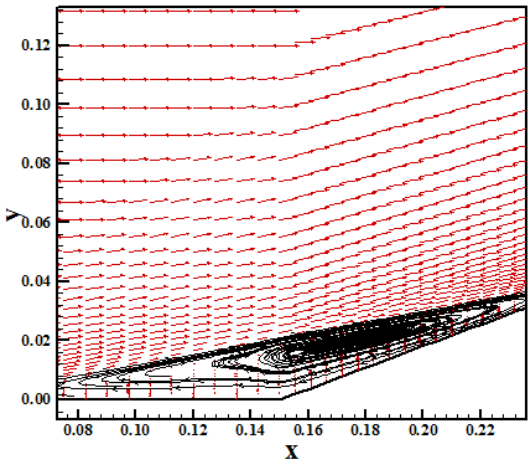

Figure 40. Circulation bubble (YWH85-BL).

Figures 39 to 42 exhibit the circulation bubble formed close to the ramp corner generated by the [3-5,10] algorithms. All schemes present the same circulation bubble extent and size.

In resume, the [12] turbulence model predicts a great extent region of boundary layer detachment and, consequently, bigger bubble size. The [12] model predicts bigger separation than the [11] model.

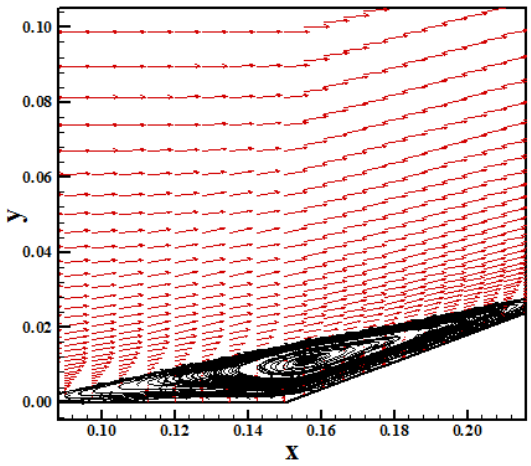

Figure 41. Circulation bubble (YK-BL).

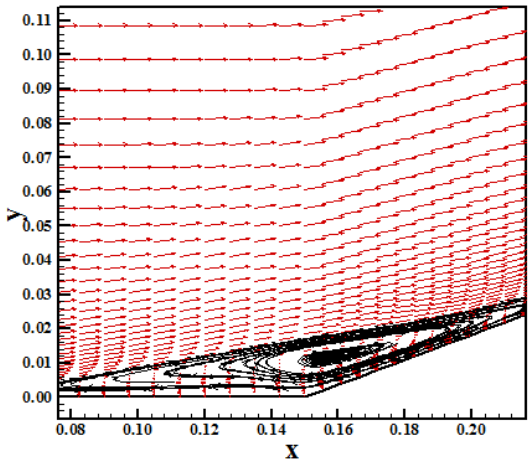

Figure 42. Circulation bubble (Yee-BL).

Sparlat and Allmaras Results. Figures 43 to 46 present the pressure contours obtained by the [3-5,10] schemes, respectively, as using the [13] turbulence model. The [3] solution captures a small boundary layer detachment, which results in a less intense weak shock wave. The [4] solution captures a bigger boundary layer detachment, which results in a more intense weak shock wave. The pressure field generated by the [3-5] schemes is more severe than that generated by the [4,10] schemes.

Figures 47 to 50 show the Mach number contours obtained by the [3-5,10] numerical schemes, respectively. The [4] solution again captures a bigger circulation bubble than the other solutions. In quantitative terms the solution generated by the [4,10] schemes is more intense than that generated by

the [3,5] schemes. Moreover, in qualitative terms the difference also exists.

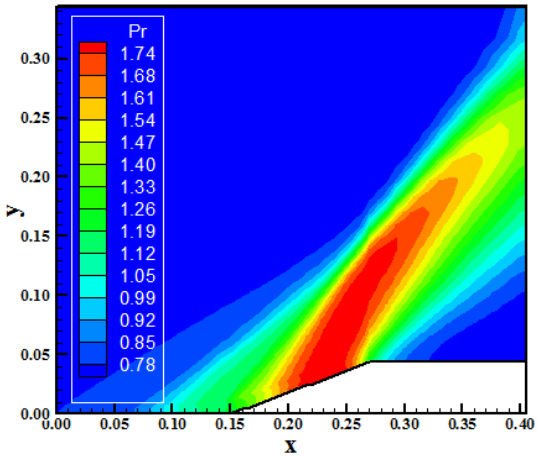

Figure 43. Pressure contours (YWH82-SA).

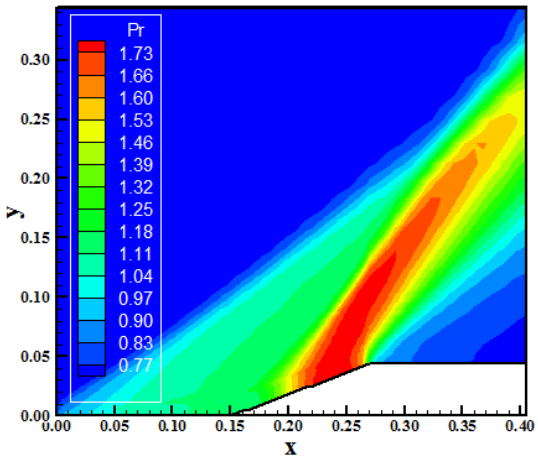

Figure 44. Pressure contours (YWH85-SA).

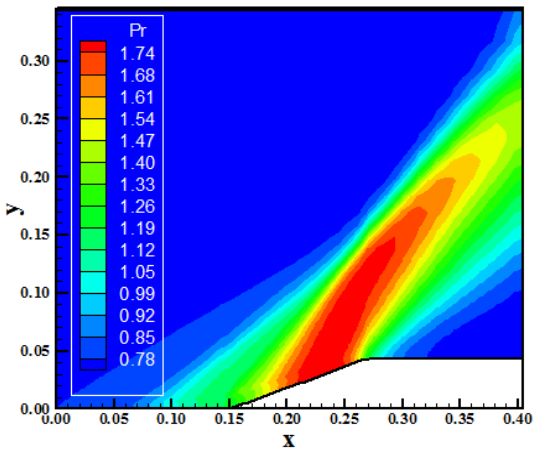

Figure 45. Pressure contours (YK-SA).

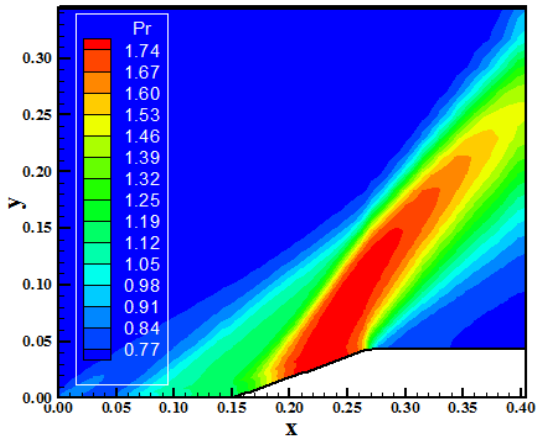

Figure 46. Pressure contours (Yee-SA).

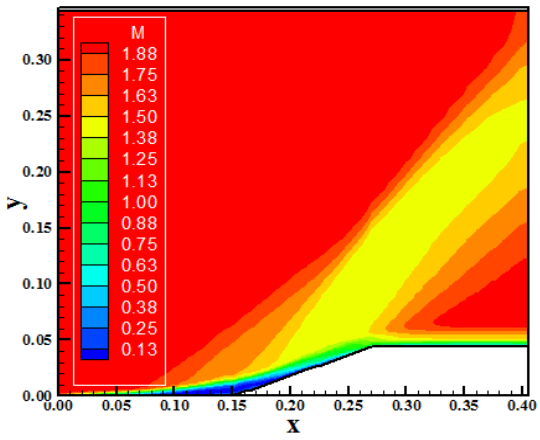

Figure 47. Mach number contours (YWH82-SA).

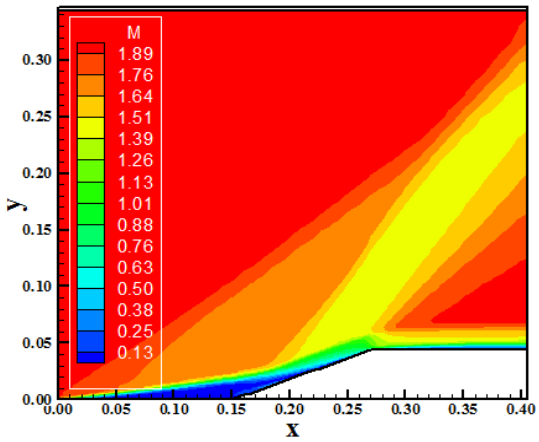

Figure 48. Mach number contours (YWH85-SA).

Figure 51 shows the wall pressure distributions obtained by the [3-5,10] algorithms. All solutions capture the circulation bubble at the ramp corner. Moreover, all pressure peaks are close to the theoretical pressure plateau.

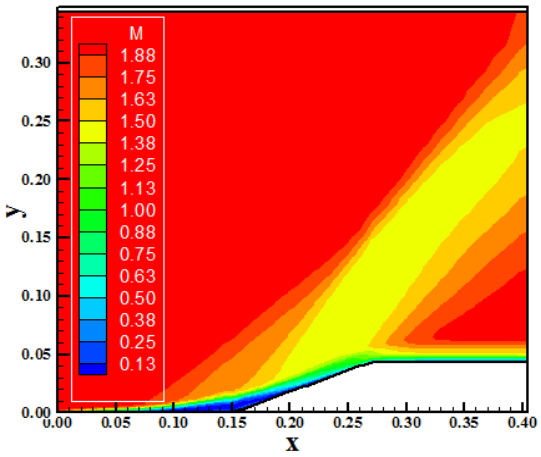

Figure 49. Mach number contours (YK-SA).

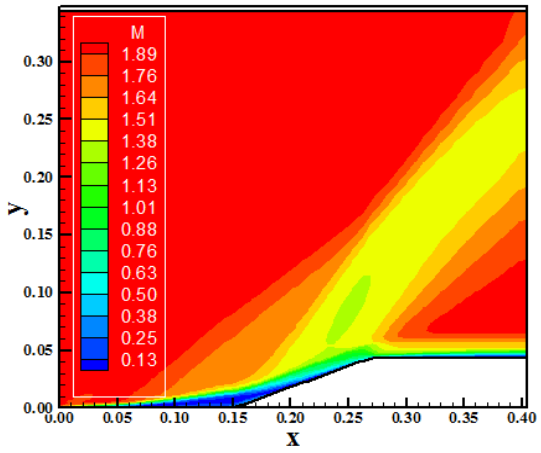

Figure 50. Mach number contours (Yee-SA).

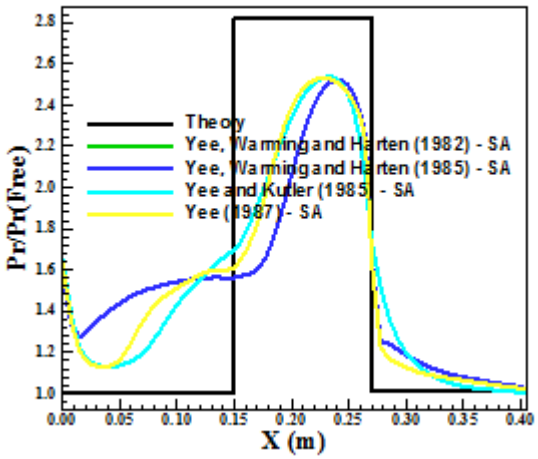

Figure 51. Wall pressure distributions.

It is important to be mentioned here that the best behavior to the pressure plateau was obtained by the [11] turbulence model in spite of the loss of physical meaning of the flow (loss of the circulation bubble formation).

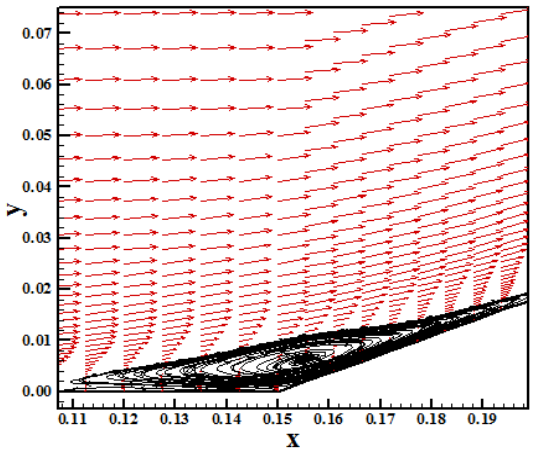

Figure 52. Circulation bubble (YWH82-SA).

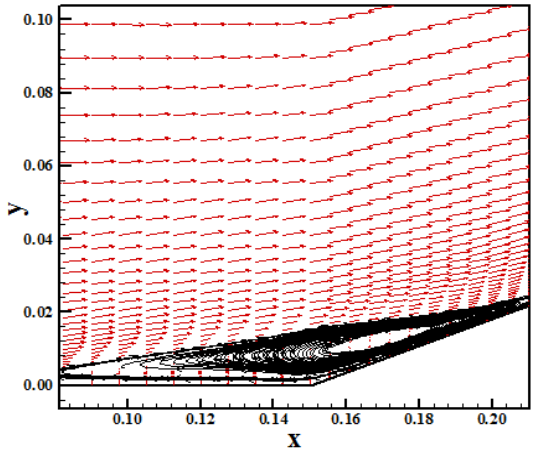

Figure 53. Circulation bubble (YWH85-SA).

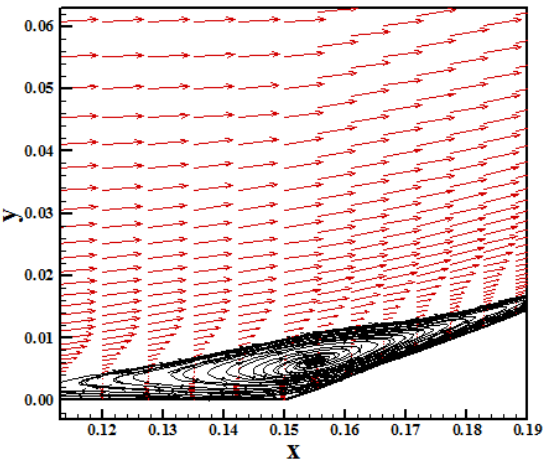

Figure 54. Circulation bubble (YK-SA).

Figures 52 to 55 exhibit the circulation bubble captured by the [3-5,10] schemes, respectively, as using the [13] turbulence model. As can be seen, all solutions generate significant bubble regions.

In resume, the [13] turbulence model predicts a less extent region of boundary layer detachment and, consequently, minor bubble size. The [13] model, an one-equation model, predicts less severe separation than the [12] model.

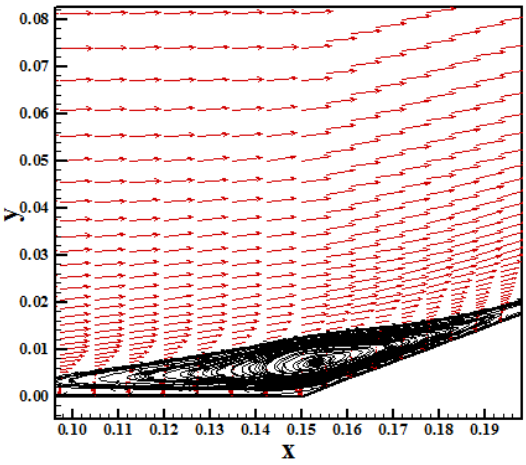

Figure 55. Circulation bubble (Yee-SA).

C. *Quantitative Analysis*

One way to quantitatively verify if the solutions generated by each scheme are satisfactory consists in determining the shock angle of the oblique shock wave, β, measured in relation to the initial direction of the flow field. [28] (pages 352 and 353) presents a diagram with values of the shock angle, β, to oblique shock waves. The value of this angle is determined as function of the freestream Mach number and of the deflection angle of the flow after the shock wave, ϕ. To $\phi = 20^{o}$ (ramp inclination angle) and to a freestream Mach number equals to 2.0, it is possible to obtain from this diagram a value to β equals to 53.0^{o}. Using a transfer in Figures 4 to 7 (laminar), Figs. 17 to 20 (CS), Figs. 30 to 33 (BL), Figs. 43 to 46 (SA), it is possible to obtain the values of β to each scheme and to each studied case, as well the respective errors, shown in Tab. 3.

Table 3. Values of the oblique shock wave angle.

Case	Lam., 2nd	CS, TVD	BL, TVD	SA, TVD
YWH82	50.5	51.5	52.0	51.5
Error	4.72	2.83	1.89	2.83
YWH85	50.0	52.0	51.6	53.5
Error	5.66	1.89	2.64	0.94
YK	50.3	53.0	51.0	51.0
Error	5.09	0.00	3.77	3.77
Yee	47.0	52.0	50.4	53.0
Error	11.32	1.89	4.91	0.00

It is possible to distinguish that the [5,10] schemes using the [11,13] turbulence models yield the best results with a zero value to the error. Hence, in terms of accuracy the [5,10] schemes are better than the other schemes.

Table 4 presents the computational data of the simulations. All schemes converged in three (3) orders. All TVD solutions of the [3,5] schemes converged with a CFL Number of 0.7, whereas all TVD solutions of the [4,10] scheme converged with CFL numbers of 0.5, 0.4 and 0.3. It is important to highlight the excellent convergence of the [3,5] schemes, converging in all cases in less than 5,500 iterations.

Table 4. Computational data.

Case	Lam., 2nd	CS, TVD	BL, TVD	SA, TVD
YWH82	0.7	0.7	0.7	0.7
	5,455	1,418	5,455	3,848
YWH85	0.4	0.3	0.3	0.3
	12,175	12,000	16,167	16,968
YK	0.7	0.7	0.7	0.7
	5,455	1,418	5,455	3,848
Yee	0.5	0.5	0.5	0.5
	8,417	4,257	8,417	7,378

VIII. Conclusions

This work, second part of this study, describes four numerical tools to perform perfect gas simulations of the laminar and turbulent viscous flow in two-dimensions. The [3-5,10] schemes are implemented to accomplish the numerical simulations. The Navier-Stokes equations, on a finite volume context and employing structured spatial discretization, are applied to solve the supersonic flow along a ramp in two-dimensions. Three turbulence models are applied to close the system, namely: [11], [12] and [13]. All schemes are TVD ones, where the [3-5] are derived from a first order upwind scheme and the [10] scheme is derived from a first order symmetrical scheme. The latter reaches TVD properties by the appropriated definition of a limited dissipation function that uses non-linear limiters. The convergence process is accelerated to the steady state condition through a spatially variable time step procedure, which has proved effective gains in terms of computational acceleration (see [14-15]). The results have shown that the [5,10] schemes yield the best results in terms of the prediction of the shock angle at the ramp. Moreover, the wall pressure distribution is also better predicted by the [10] algorithm.

References

[1] S. K. Godunov, A Finite Difference Method for the Numerical Computation of Discontinuous Solutions of the Equations of Fluid Dynamics, *Math. Sb.*, Vol. 47, 1959, p. 271.

[2] A. Harten, High Resolution Schemes for Hyperbolic Conservation Laws, *Journal of Computational Physics*, Vol. 49, 1983, pp. 357-393.

[3] H. C. Yee, R. F. Warming, and A. Harten, A High-Resolution Numerical Technique for Inviscid Gas-Dynamic Problems with Weak Solutions, *Proceedings of the 8th International Conference on Numerical Methods in Fluid Dynamics*, E. Krause, Editor, Lecture

Notes in Physics, Springer-Verlag, Berlim, Germany, Vol. 170, 1982, pp. 546-552.
[4] H. C. Yee, R. F. Warming, and A. Harten, Implicit Total Variation Diminishing (TVD) Schemes for Steady-State Calculations, *Journal of Computational Physics*, Vol. 57, No. 3, 1985, pp. 327-360.
[5] H. C. Yee, and P. Kutler, Application of Second-Order-Accurate Total Variation Diminishing (TVD) Schemes to the Euler Equations in General Geometries, *NASA-TM-85845*, 1985.
[6] R. W. MacCormack, The Effect of Viscosity in Hypervelocity Impact Cratering, *AIAA Paper 69-354*.
[7] H. C. Yee, A Class of High Resolution Explicit and Implicit Shock-Capturing Methods, *NASA TM-101088*, 1989.
[8] Roe, P. L., Characteristic-based Schemes for the Euler Equations, *Annual Review of Fluid Mechanics*, Vol. 18, 1986, pp. 337-365.
[9] G. Moretti, 1987, Computation of Flows with Shocks, *Annual Review of Fluid Mechanics*, Vol. 19, 1987, pp. 313-337.
[10] H. C. Yee, Construction of Explicit and Implicit Symmetric TVD Schemes and Their Applications, *Journal of Computational Physics*, Vol. 68, 1987, pp. 151-179.
[11] T. Cebeci, and A. M. O. Smith, A Finite-Difference Method for Calculating Compressible Laminar and Turbulent Boundary Layers, *Journal of Basic Engineering*, Trans. ASME, Series B, Vol. 92, No. 3, 1970, pp. 523-535.
[12] B. D. Baldwin, and H. Lomax, Thin Layer Approximation and Algebraic Model for Separated Turbulent Flows, *AIAA Paper 78-257*, 1978.
[13] P. R. Sparlat, and S. R. Allmaras, A One-Equation Turbulence Model for Aerodynamic Flows, *AIAA Paper 92-0439*, 1992.
[14] E. S. G. Maciel, Analysis of Convergence Acceleration Techniques Used in Unstructured Algorithms in the Solution of Aeronautical Problems – Part I, *Proceedings of the XVIII International Congress of Mechanical Engineering (XVIII COBEM)*, Ouro Preto, MG, Brazil, 2005. [available in CD-ROM]
[15] E. S. G. Maciel, Analysis of Convergence Acceleration Techniques Used in Unstructured Algorithms in the Solution of Aerospace Problems – Part II", *Proceedings of the XII Brazilian Congress of Thermal Engineering and Sciences (XII ENCIT)*, Belo Horizonte, MG, Brazil, 2008. [available in CD-ROM]
[16] E. S. G. Maciel, Laminar and Turbulent Simulations of Several TVD Schemes in Two-Dimensions – Part I, *Submitted to WSEAS Transactions on Computers* (under review).
[17] E. S. G. Maciel, Comparison Between the Yee, Warming and Harten and the Hughson and Beran High Resolution Algorithms in the Solution of the Euler Equations in Two-Dimensions – Theory, *Proceedings of the XXVII Iberian Latin American Congress on Computational Methods in Engineering (XXVII CILAMCE)*, Belém, Pará, Brazil, 2006. [available in CD-ROM]
[18] E. S. G. Maciel, Comparison Between the Yee, Warming and Harten and the Hughson and Beran High Resolution Algorithms in the Solution of the Euler Equations in Two-Dimensions – Results, *Proceedings of the XXVII Iberian Latin American Congress on Computational Methods in Engineering (XXVII CILAMCE)*, Belém, Pará, Brazil, 2006. [available in CD-ROM]
[19] E. S. G. Maciel, and E. M. Ferreira, TVD and ENO Applications to Supersonic Flows in 2D – Part I, Submitted to *WSEAS Transactions on Mathematics* (under revision).
[20] E. S. G. Maciel, Solutions of the Euler and the Laminar and Turbulent Navier-Stokes Equations in Two-Dimensions Using TVD and ENO Algorithms, *WSEAS Transactions on Mathematics*, Vol. 11, Issue 6, 2012, pp. 478-500.
[21] E. S. G. Maciel, Explicit and Implicit TVD High Resolution Schemes in 2D, *WSEAS Transactions on Applied and Theoretical Mechanics*, Vol. 7, Issue 3, 2012, pp. 182-109.
[22] E. S. G. Maciel, Explicit and Implicit TVD High Resolution Schemes in 2D – Theory, *Proceedings of the X Symposium of Computational Mechanics (X SIMMEC)*, Belo Horizonte, MG, Brazil, 2012. [available in CD-ROM]
[23] E. S. G. Maciel, Explicit and Implicit TVD High Resolution Schemes in 2D – Results, *Proceedings of the X Symposium of Computational Mechanics (X SIMMEC)*, Belo Horizonte, MG, Brazil, 2012. [available in CD-ROM]
[24] E. S. G. Maciel, Explicit and Implicit TVD and ENO High Resolution Algorithms Applied to the Euler and Navier-Stokes Equations in Three-Dimensions – Theory, *Proceedings of the XX International Congress of Mechanical Engineering (XX COBEM)*, Gramado, RS, Brazil, 2009. [available in CD-ROM]
[25] E. S. G. Maciel, Explicit and Implicit TVD and ENO High Resolution Algorithms Applied to the Euler and Navier-Stokes Equations in Three-Dimensions – Results, *Proceedings of the XX International Congress of Mechanical Engineering (XX COBEM)*, Gramado, RS, Brazil, 2009. [available in CD-ROM]

Edisson S. G. Maciel (F'14), born in 1969, february, 25, in Recife, Pernambuco. He is a Mechanical Engineering undergraduated by UFPE in 1992, in Recife, PE, Brazil; Mester degree in Thermal Engineering by UFPE in 1995, in Recife, PE, Brazil; Doctor degree in Aeronautical Engineering by ITA in 2002, in São José dos Campos, SP, Brazil; and Post-Doctor degree in Aeronautical Engineering by ITA in 2009, in São José dos Campos, SP, Brazil.

Actually, he is doing a new post-doctorate curse in Aerospace Engineering at ITA. The last researches are based on thermochemical non-equilibrium reentry simulations in Earth and thermochemical non-equilibrium entry simulations in Mars. They are: Maciel, E. S. G., and Pimenta, A. P., "Thermochemical Non-Equilibrium Reentry Flows in Two-Dimensions – Part I', WSEAS Transactions on Mathematics, Vol. 11, Issue 6, June, pp. 520-545, 2012; Maciel, E. S. G., and Pimenta, A. P., "Thermochemical Non-Equilibrium Entry Flows in Mars in Two-Dimensions – Part I', WSEAS Transactions on Applied and Theoretical Mechanics, Vol. 8, Issue 1, January, pp. 26-54, 2013; and he has three published books, the first one being: Maciel, E. S. G., "Aplicações de Algoritmos Preditor-Corretor e TVD na Solução das Equações de Euler e de Navier-Stokes em Duas Dimensões", Recife, PE, Editor UFPE, 2013. He is interested in the Magnetogasdynamic field with applications to fluid dynamics and in the use of ENO algorithms.